Development of the γ' Stability in Co–Al–W Alloys at 800 °C by Alloying with Carbon

H. KAMALI, R.D. FIELD, A.J. CLARKE, S. HOSSEIN NEDJAD, and M.J. KAUFMAN

The microstructures and hardnesses of Co–10Al–9W–1C, Co–7Al–5W–1C, and Co–7Al–5W (at. pct) alloys are reported. Homogenization of the Co–10Al–9W–1C alloy was unsuccessful at 1300 °C and both B2–CoAl and η carbide phases remained in the interdendritic regions. However, the lower-solute Co–7Al–5W–1C and Co–7Al–5W alloys did homogenize at 1300 °C. Upon aging the Co–10Al–9W–1C alloy at 800 °C, the undissolved η carbide transformed into W-supersaturated $D0_{19}$–Co_3W phase and subsequently into γ'-$Co_3(Al,W)$ phase, indicating the stability of the γ' phase in the C-doped alloy in contrast with ternary Co–Al–W alloys where the γ' is metastable. Also, high γ' volume fractions and low γ' coarsening rates were revealed by transmission electron microscopy in the various Co–Al–W–C alloys. These observations are explained by the effects of C on the phase equilibria and the γ/γ' composition in the Co–Al–W system. Finally, the microhardness is increased while the density is decreased by alloying with C, which could result in higher specific strengths in the C-doped alloys.

I. INTRODUCTION

WHILE Ni-base superalloys are used more commonly in the various industries due to their higher strength, better strength retention,[1] and lower cost than commercial Co-base alloys, there remains a desire to improve the strength properties of Co-base alloys given their desirable attributes, such as higher melting temperatures, outstanding hot corrosion resistance in contaminated gas turbine atmospheres,[1] better weldability and wear resistance,[2] and superior thermal fatigue resistance[3] compared to Ni-base alloys. In this regard, precipitation hardening is the preferred approach for improving the strength of Co-base alloys with the goal of producing Co-base superalloys with good elevated strength retention.

A κ-Co_3AlC phase with the $E2_1$ (perovskite) structure was reported in 1958 as a geometrically close-packed phase in the Co–Al–C system by Huetter and Stadelmaier.[4] However, discontinuous precipitation of the κ due to high lattice misfit between the κ and Co matrix (about 3.9 pct) makes strength retention impossible in these alloys.[5] Later, the formation of a $Co_3(Al,W)$ phase with the $L1_2$ structure was reported in the Co–Al–W system by Lee[6] in 1971. Later, Sato, et al.[7] in 2006 determined the ternary isotherms in the Co–Al–W system and showed the existence of the γ'-$Co_3(Al,W)$ in Co–Al–W alloys at 900 °C. Since the report of Sato et al.,[7] significant efforts have been made to understand phase stability,[8–13] deformation behavior,[14–16] high-temperature mechanical[17–21] and environmental properties[22–24] of γ'-strengthened Co-base alloys. In some of these studies, it was determined that this γ' phase is metastable[8,10–13] and has relatively low solvus temperatures compared to the γ' in Ni-base alloys, thereby limiting its industrial applicability. A further drawback is the relatively high densities of Co–Al–W alloys due to their high W contents.[25]

Given that the Co_3Al ($L1_2$) is unstable in the Co–Al binary system,[26] but that it does form a metastable phase, i.e., $Co_3(Al,W)$, in the Co–Al–W system,[7] and noting that the structurally similar κ-Co_3AlC phase in the Co–Al–C system is stable,[27] it was speculated that C additions might lead to stabilization of the γ' phase in Co–Al–W–C alloys. Freund, et al.[28] reported a lower W content for the γ' in the microstructure of a Co–10Al–7.5W–5C (at. pct) alloy at 900 °C compared with ternary Co–Al–W alloys, presumably due to C partitioning to the γ', and suggested that this could indicate an increase in γ' stability relative to C-free alloys. However, it has also been shown that

H. KAMALI is with the Department of Metallurgical and Materials Engineering, College of Applied Science and Engineering, Colorado School of Mines, Golden, CO 80401 and also with the Department of Materials Engineering, Sahand University of Technology, P.O. Box 51335-1996, Tabriz, Iran. R.D. FIELD, A.J. CLARKE, and M.J. KAUFMAN are with the Department of Metallurgical and Materials Engineering, College of Applied Science and Engineering, Colorado School of Mines. Contact e-mail: mkaufman@mines.edu S. HOSSEIN NEDJAD is with the Department of Materials Engineering, Sahand University of Technology.

discontinuous precipitation of the κ and/or B2–CoAl phases occurs in the Co–10Al–7.5W–5C (at. pct) alloy, along with discontinuous precipitation/coarsening of the γ' precipitates in the matrix during aging at 900 °C.[28]

In the present study, the ratio of C to W was decreased in an effort to (1) avoid the formation of the κ phase, and (2) assess the effects of C on the microstructural evolution, phase stability, and age hardening behavior of a Co–10Al–9W (at. pct) alloy upon aging at 800 °C. Also, the effects of a 1 at. pct C addition on the microstructure and hardness of a Co–7Al–5W (at. pct) alloy during aging at 800 °C were examined for comparison.

II. EXPERIMENTAL METHODS

Buttons of Co–10Al–9W–1C, Co–7Al–5W–1C, and Co–7Al–5W (at. pct) (all of the compositions in this study are in at. pct) were cast by non-consumable arc melting of commercially pure raw materials in a purified (Ti gettered) argon atmosphere. The samples were remelted at least seven times in an attempt to ensure compositional homogeneity and dissolution of the tungsten and graphite in the alloy melts. In order to ensure dissolution of C in the melt occurred, standard samples were cut from cast buttons and their C contents were measured using a LECO® carbon analyzer. Also, energy-dispersive X-ray spectroscopy (EDS) analyses conducted at an accelerating voltage of 20 kV and on large areas of the samples indicated that the compositions of the alloys were close to their nominal compositions. The specimens were then encapsulated in quartz tubes backfilled with high purity argon, and heat treated in a resistance furnace at 1300 °C for 12 hours followed by water quenching. Sections from the heat-treated samples were cut and encapsulated in quartz tubes with inert Ar atmosphere and aged at 800 °C. The Co–10Al–9W–1C alloy was aged for 1, 16, 64, and 256 hours, and the Co–7Al–5W–1C and Co–7Al–5W alloys were aged for 16 and 64 hours, and then water quenched. Standard metallographic techniques were used to mount and polish the specimens. The final polish of the samples was done using a 0.05 μm colloidal silica solution. Scanning electron microscopy (SEM) studies were conducted using an FEI Quanta 600i Environmental SEM and a JEOL JSM-7000F Field Emission SEM (FESEM), both operated at 20 kV. Transmission electron microscopy (TEM) samples of the Co–7Al–5W–1C and Co–7Al–5W alloys aged for 16 hours were prepared using a focused ion beam (FIB) milling technique on a Dual-Beam FIB instrument (FEI Helios Nanolab 600i FIB) using a Ga ion beam. The ion beam thinning was carried out initially using 30 kV ions and finally using 2 kV ions to reduce the damage caused by the higher energy ions. The other TEM samples were prepared by twin-jet electropolishing in a solution of 5 vol pct perchloric acid in methanol at − 30 °C and 18 V. Conventional and scanning TEM (STEM) analyses were conducted on a Philips CM12 TEM operated at 120 kV and an FEI Talos F200X CTEM/STEM operated at 200 kV equipped with an integrated EDS system with four silicon drift detectors (SDDs), respectively. Area fractions and sizes of the γ' precipitates in each sample were obtained by applying standard protocols to the TEM micrographs using ImageJ ™ software.[29] For the γ' precipitate sizes, the average value and ± 1 standard deviation range were calculated. Microhardness measurements were conducted using 300 g load in a LECO® Vickers microhardness machine. At least 12 hardness measurements were taken at different positions of each sample and the average, minimum, and maximum values were determined.

III. RESULTS

A. *Microstructural Characterization*

1. *Co–10Al–9W–1C alloy*

The microstructure of the as-cast Co–10Al–9W–1C alloy (Figure 1(a)) consists of a dendritic solidification structure with interdendritic segregation, where the latter contains a higher Z (bright) and a lower Z (dark) phase relative to the primary dendrites. Upon heat treatment at 1300 °C for 12 h (Figure 1(b)), the structure of the Co–10Al–9W–1C alloy was expected to become single phase, based on the Co–Al–W ternary isotherm at 1300 °C.[8] Also, according to the average size of the dendritic as-cast microstructure (about 20 μm) and the known diffusivity of W (expected to be rate controlling) in the γ-Co matrix at 1300 °C (1.1×10^{-14} m^2 s^{-1}[30]), and also the typical homogenization treatment for Co–Al–W alloys,[13,17,18,21,22,28,31,32] this alloy was expected to homogenize during this heat treatment. However, the higher Z and lower Z phases remained in the microstructure. The results of the EDS point analyses of the higher Z, lower Z, and dendritic regions are shown in Table I. It is noted that the carbon contents of the phases were not measured using EDS, due to (a) its low fluorescent yield and (b) the carbon contamination that typically occurs on the surface during spot EDS analysis. Further, by ignoring the C in the EDS analysis, it was possible to more accurately quantify the Al and W contents of the phases. Based on the EDS (Table I) and electron diffraction analyses (described below), the higher Z, lower Z, and dendritic phases are η-Co$_3$W$_3$C/Co$_6$W$_6$C (exact composition was not determined due to the low accuracy of EDS for C, and their similar crystal structures[33]), B2–CoAl, and γ, respectively. Thus, it is clear that the addition of 1 pct C changes the phase equilibria in the Co–Al–W system significantly.

Selected area diffraction (SAD) patterns systematically taken from four different zone axes of the η phase (higher Z interdendritic regions) in the microstructure of the Co–10Al–9W–1C alloy heat treated at 1300 °C for 12 hours (Figure 1(b)) are shown in Figure 2. The SAD patterns in Figures 2(a) through (d) are consistent with the diffraction patterns along the [013], [011], [$\bar{1}$11], and [001] zone axes, respectively, of the η-Co$_3$W$_3$C/Co$_6$W$_6$C phase with the Fd-3m (No. 227) space group.[34–36] The 200 reflections in the SAD patterns of Figures 2(a) and (b) are forbidden reflections in the Fd-3m (No. 227)
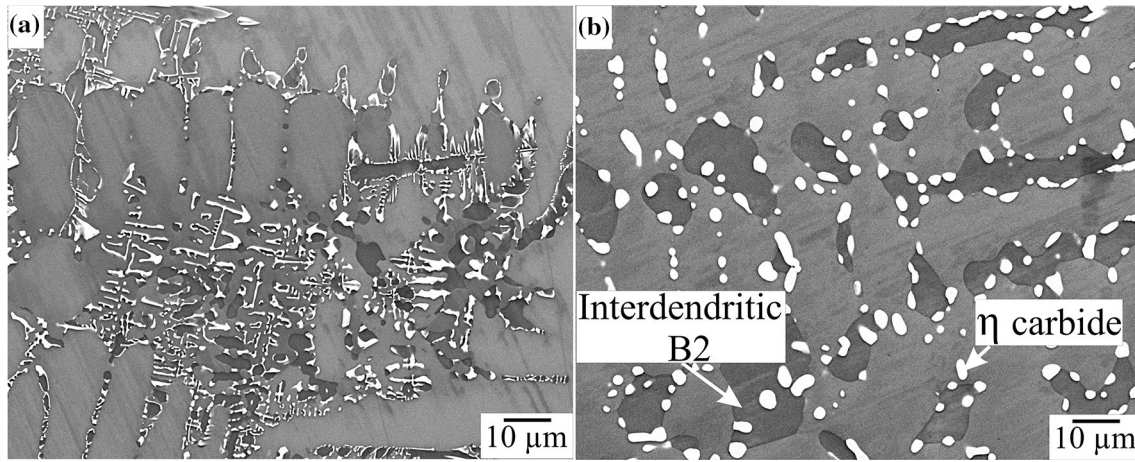
Fig. 1—FESEM images of the Co–10Al–9W–1C alloy in the as-cast condition (*a*), and after heat treatment at 1300 °C for 12 h (*b*).

Table I. FESEM EDS Point Results From the Higher *Z*, Lower *Z*, and Dendritic Phases in the Microstructure of the Co–10Al–9W–1C Alloy After Heat Treatment at 1300 °C

Phase	Elemental Composition (At. Pct)		
	Co	Al	W
Higher *Z*	47.5	7.6	44.9
Lower *Z*	74.4	21.3	4.3
Dendritic	82.6	12.3	5.1

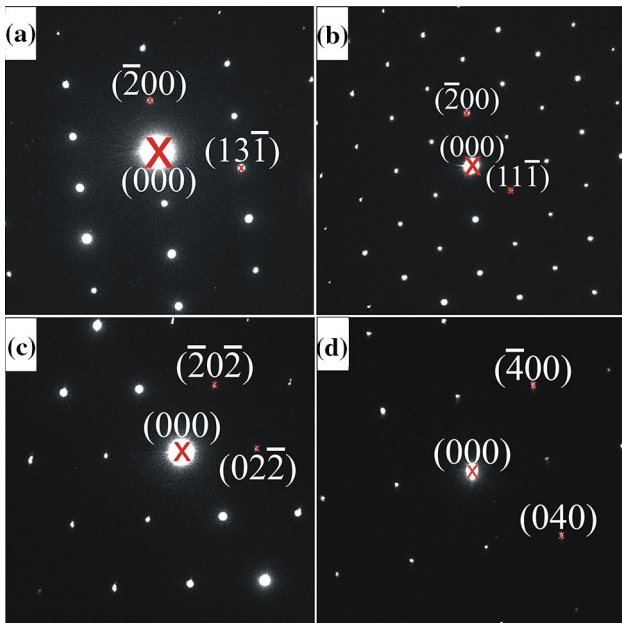
Fig. 2—SAD patterns of the interdendritic diamond cubic η phase existing in the 1300 °C for 12 h heat-treated Co–10Al–9W–1C sample taken from: (*a*) [013], (*b*) [011], (*c*) [$\bar{1}$11], and (*d*) [001] zone axes.

space group[36] and are due to double diffraction. As expected, they are absent in the [001] zone axis (Figure 2(d)), consistent with this space group.
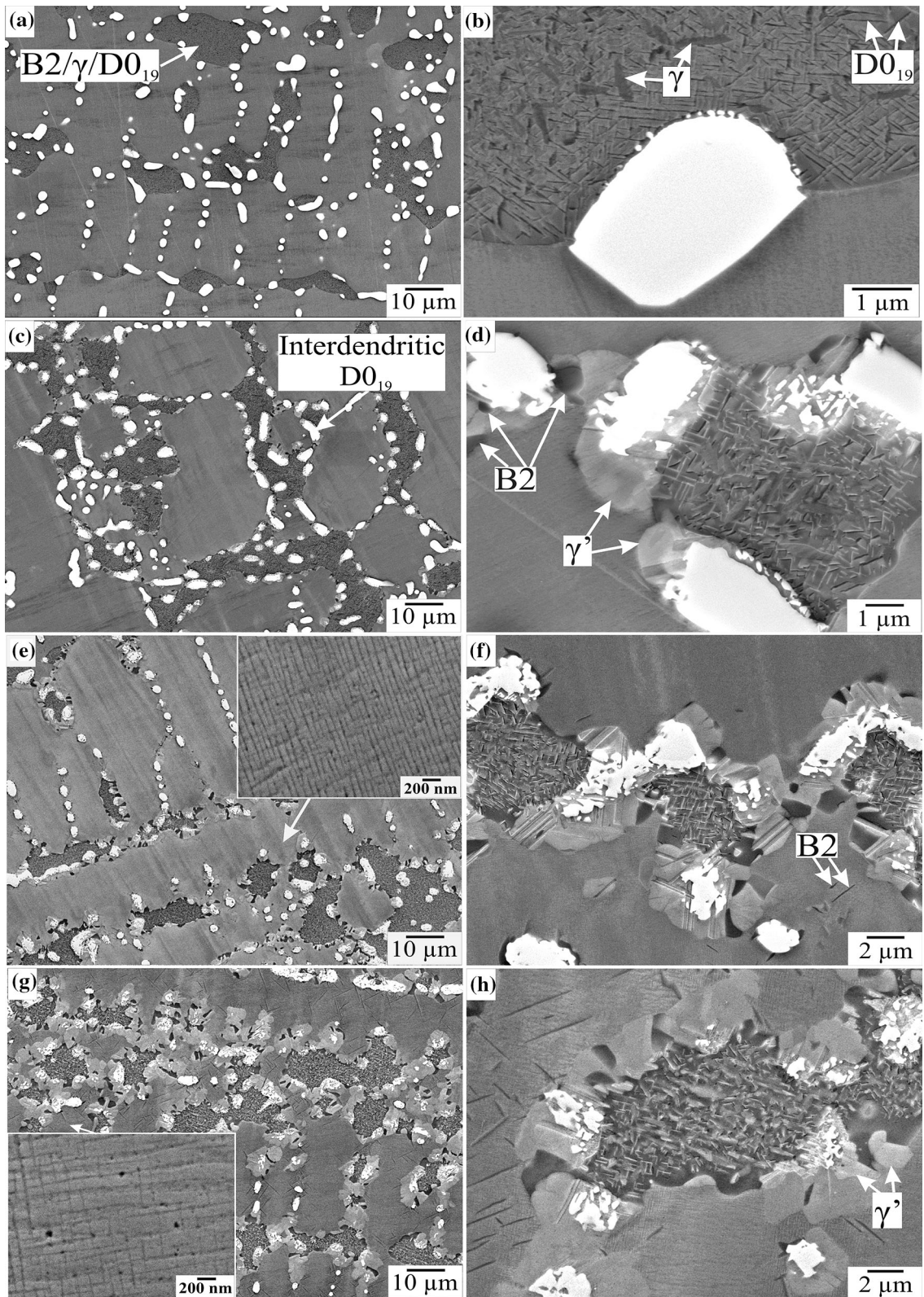
Subsequent to the 1300 °C, 12 hours "homogenization" treatment, the samples were aged at 800 °C for 1, 16, 64, and 256 hours (Figure 3). The precipitation of the γ and $D0_{19}$–Co_3W in the interdendritic B2 phase is seen in Figures 3(a) and (b), due to the large decrease in solid solubility in the B2 phase between 1300 °C and 800 °C. It is noted that the $D0_{19}$ precipitates exhibit a darker contrast than the interdendritic B2 matrix in Figure 3(b), since the $D0_{19}$ precipitates have been removed from the matrix during sample preparation (probably due to being preferentially etched by the colloidal silica solution). Also, based on evidence provided in the following, the higher *Z* η carbide in the interdendritic regions transforms into the $D0_{19}$ phase at 800 °C; this has not been reported in the literature previously. The images in Figures 3(c) through (h) indicate that the product $D0_{19}$ particles gradually decomposed into a γ' layer growing toward the interdendritic B2 and dendritic regions during aging; consequently, the thicknesses of the γ' layers surrounding the $D0_{19}$ particles increase during $D0_{19}$ decomposition. Also, the formation of blocky B2 phase at the interface between the γ' layers and the dendritic regions (Figures 3(c) through (h)), and precipitation of both fine γ' precipitates with a high volume fraction and needle-like B2 precipitates in the dendritic γ phase (Figures 3(e) through (h)) occurred during aging at 800 °C.

The EDS point results from the coarse $D0_{19}$, blocky B2, and γ' layers in the microstructure of the Co–10Al–9W–1C alloy aged at 800 °C for 256 hours (Figures 3(g) and (h)) are summarized in Table II. Comparing Tables I and II, although the W and Al contents of the product $D0_{19}$ phase are lower than those of the parent η carbide, the W content of the $D0_{19}$ phase is still higher than its equilibrium content (~25 pct)[11] even after 256 hours aging at 800 °C.

Bright-field TEM images and corresponding SAD patterns in Figure 4 exhibit the interdendritic B2 (lower *Z* phase in Figures 3(g) and (h)) and $D0_{19}$ (higher *Z* phase in Figures 3(g) and (h)) regions in the Co–10Al–9W–1C alloy aged at 800 °C for 256 hours.

Fig. 3—FESEM microstructures of the Co–10Al–9W–1C alloy aged at 800 °C for 1 h (*a* and *b*), 16 h (*c* and *d*), 64 h (*e* and *f*), and 256 h (*g* and *h*).

Furthermore, the interdendritic B2 region contains fine γ and $D0_{19}$ precipitates after aging at 800 °C. The higher magnification bright-field images in Figure 4 show that

the $D0_{19}$ particles are faulted, and that the density of the faults in the coarse $D0_{19}$ phase is higher than that in the fine $D0_{19}$ precipitates. Based on the higher magnification

Phase	Elemental Composition (At. Pct)		
	Co	Al	W
D0$_{19}$ (Coarse)	53.8	3.9	42.3
B2 (Blocky)	60.0	37.7	2.3
γ' (Layer)	77.5	12.4	10.1

image of the coarse D0$_{19}$ phase (upper-right image), these faults are visible under $g = 0002$ two-beam conditions and lie on the basal planes of the hexagonal D0$_{19}$ structure. It has been reported that there are two sets of displacements in the D0$_{19}$ structure[37]; one set consists of displacements on the basal plane which can lead to anti-phase boundaries (APBs), complex intrinsic stacking faults (CISFs), and superlattice intrinsic stacking faults (SISFs), with the displacement vectors of $R_{APB} = 1/6\langle\bar{1}2\bar{1}0\rangle$, $R_{CISF} = 1/6\langle01\bar{1}0\rangle$ and $R_{SISF} = 1/3\langle\bar{1}100\rangle$, respectively. The other set involves translations
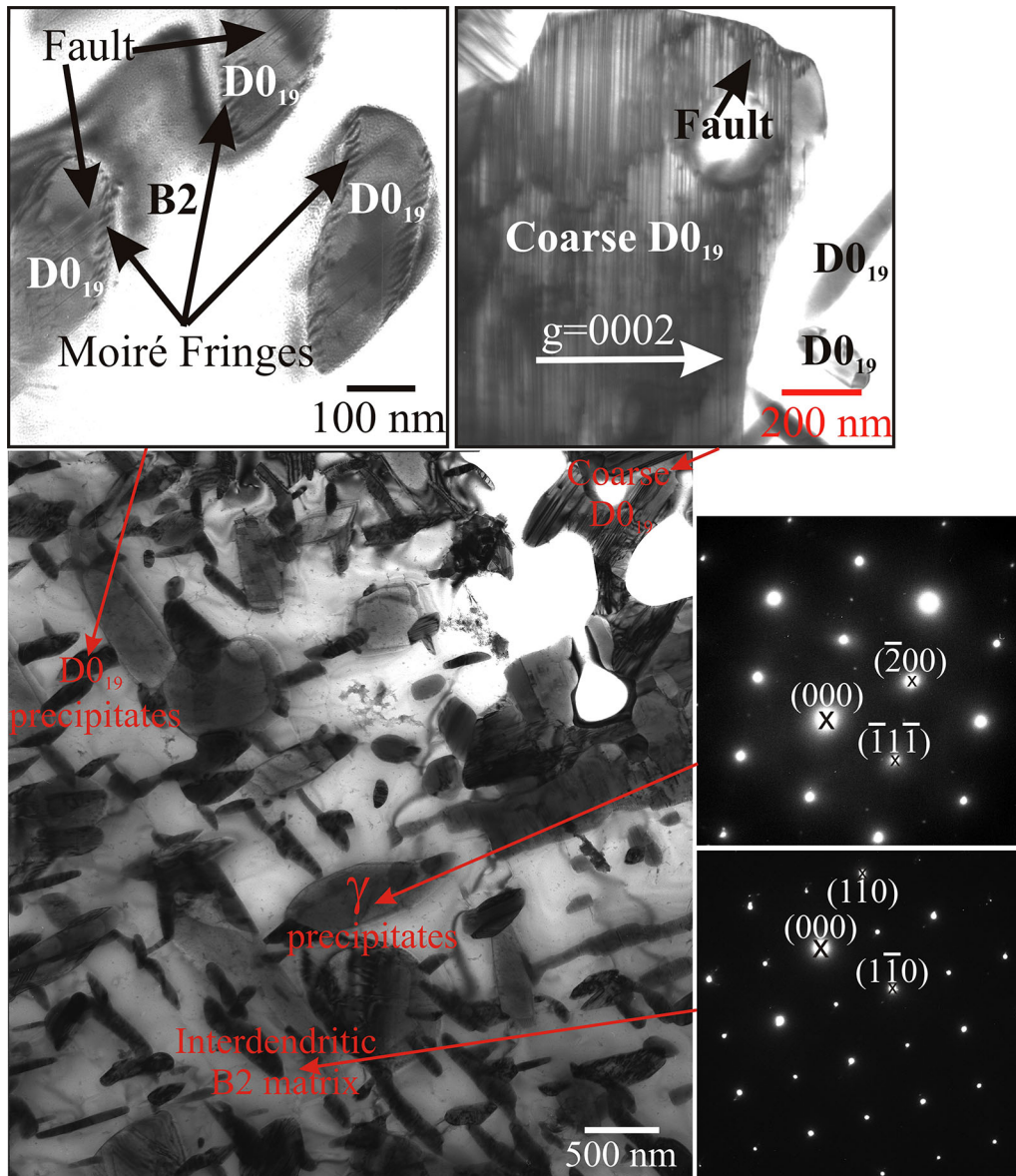

Fig. 4—Bright-field TEM images and corresponding SAD patterns of the interdendritic phases in the microstructure of the Co–10Al–9W–1C alloy aged at 800 °C for 256 h.
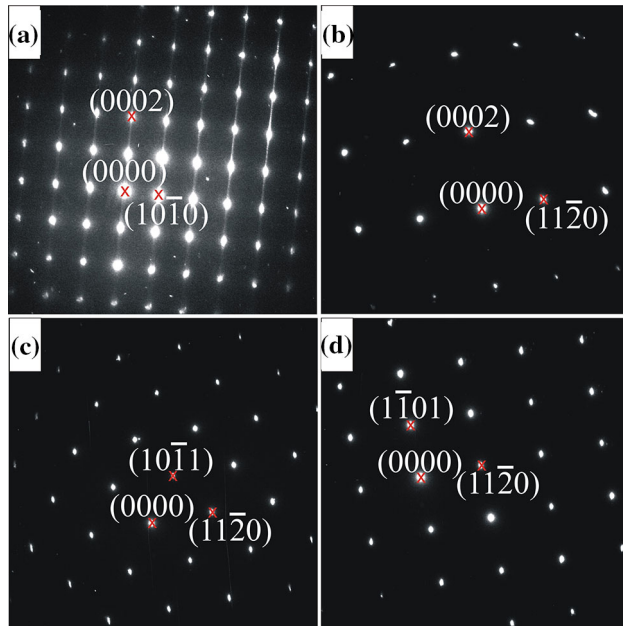
Fig. 5—SAD patterns of the coarse interdendritic $D0_{19}$ phase in the Co–10Al–9W–1C alloy aged at 800 °C for 256 h (Fig. 4) taken from: (a) [1$\bar{2}$10], (b) [1$\bar{1}$00], (c) [1$\bar{1}$0$\bar{1}$], and (d) [1$\bar{1}$0$\bar{2}$] zone axes.
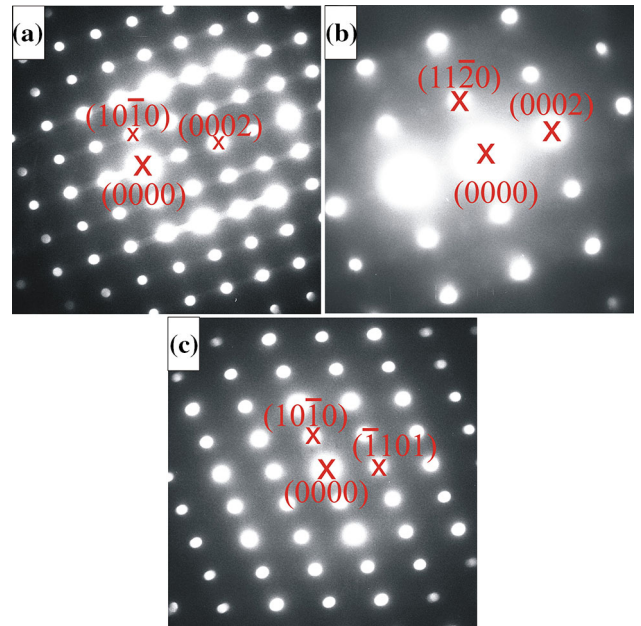

Fig. 6—Microdiffraction patterns of the fine $D0_{19}$ precipitates inside the interdendritic B2 matrix in the Co–10Al–9W–1C sample aged at 800 °C for 256 h (Fig. 4) taken from: (a) [1$\bar{2}$10], (b) [1$\bar{1}$00], and (c) [1$\bar{2}$13] zone axes.

perpendicular to the basal plane, which can produce complex stacking faults and superlattice stacking faults with the displacement vectors of $R = 1/6\langle 01\bar{1}3\rangle$ and $R = 1/6\langle\bar{2}203\rangle$, respectively.[37] Based on the visibility criteria ($g\cdot R \neq 0$), the displacement vector of the visible faults in Figure 4 under $g = 0002$ diffracting conditions is consistent with $R = 1/6\langle\bar{2}203\rangle$ (superlattice stacking faults) or $R = 1/6\langle 01\bar{1}3\rangle$ (complex stacking faults). The formation of the superlattice stacking faults in the $D0_{19}$ phase has been shown to be energetically favorable.[37] Thus, the observed faults in the structure of the coarse $D0_{19}$ phase are most likely the superlattice stacking faults with the displacement vector of $R = 1/6\langle\bar{2}203\rangle$, which is in fact equivalent to a 180° rotation of the hexagonal $D0_{19}$ crystal on the basal plane around the [0001] axis.[37] Also, Moiré fringes are evident at the edges of the fine $D0_{19}$ precipitates in the upper-left image in Figure 4. These fringes formed in the bright-field TEM image where the fine $D0_{19}$ precipitates and the interdendritic B2 matrix overlapped, due to interference of diffracting lattice planes of the $D0_{19}$ and B2 crystals, which have different spacings or orientations.[38]

SAD patterns systematically taken from four different zone axes of the coarse $D0_{19}$ phase (higher Z interdendritic regions) in the microstructure of the alloy aged at 800 °C for 256 hours (Figures 3(g) and (h), and 4) are depicted in Figure 5. The SAD patterns in Figures 5(a) through (d) are consistent with the diffraction patterns along the [1$\bar{2}$10], [1$\bar{1}$00], [1$\bar{1}$0$\bar{1}$], and [1$\bar{1}$0$\bar{2}$] zone axes, respectively, of the $D0_{19}$–Co_3W phase with the $P6_3/mmc$ (No. 194) space group.[34–36] The streaking of diffraction spots in Figure 5(a) along $g = 0002$ is consistent with the existence of the faults on the basal planes of the coarse $D0_{19}$ particles (Figure 4). Also, the forbidden

0001 spots are due to double diffraction in the [1$\bar{2}$10] zone axis (Figure 5(a)).

Figure 6 shows microdiffraction patterns systematically taken from three different zone axes of the fine $D0_{19}$ precipitates inside the B2 interdendritic phase in the sample aged at 800 °C for 256 hours (Figure 4). The microdiffraction patterns in Figures 6(a) through (c) are consistent with the diffraction patterns along the [1$\bar{2}$10], [1$\bar{1}$00], and [1$\bar{2}$13] zone axes, respectively, of the $D0_{19}$ phase.[34–36] Again, the streaking in Figure 6(a) is related to the basal faults in the $D0_{19}$ precipitates as are visible in the higher magnification image in Figure 4 (upper left).[36] The faults in the $D0_{19}$ precipitates are likely SFs or APBs.[37]

Centered dark-field TEM images and corresponding SAD patterns taken from the dendritic regions of the Co–10Al–9W–1C samples heat treated at 1300 °C for 12 hours (Figure 7(a)) and subsequently aged at 800 °C for 1, 16, 64, and 256 hours are shown in Figures 7(b) through (e). As seen in Figure 7(a), fine γ' precipitates in the dendritic regions formed upon quenching from 1300 °C to room temperature. These precipitates coarsen during subsequent aging at 800 °C, as expected (Figures 7(b) through (e)). Also, the morphologies of the γ' precipitates change from spherical to cuboidal, which become aligned in the soft $\langle 001\rangle$ directions of the γ matrix during aging, due to elastic strain energy effects.[39] The measured γ' area fractions were determined to be ~78 pct by analyzing the dark-field images in Figures 7(c) through (e); this is close to a γ' area fraction of ~70 pct reported in the microstructure of a Co–10Al–10W ternary alloy aged at 800 °C.[32]

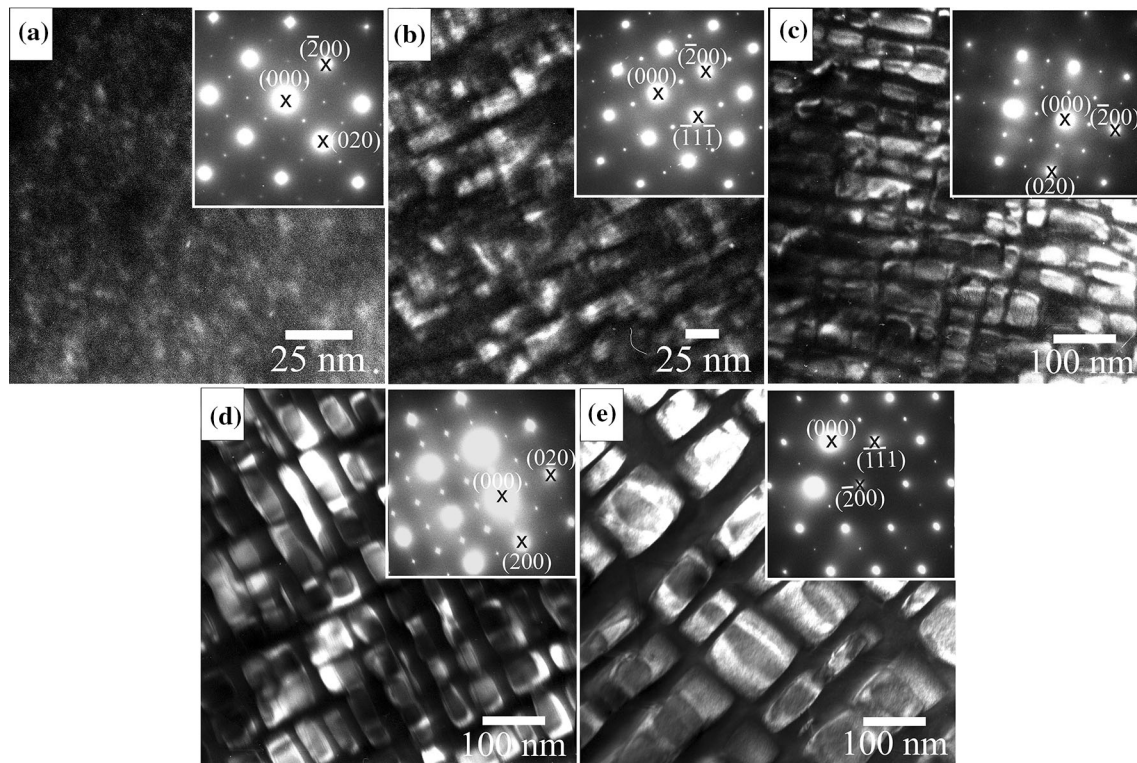Bright-field two-beam images in Figures 8(a) and (b) suggest that, in some dendritic regions of the

Fig. 7—Dark-field TEM images and corresponding SAD patterns of the dendritic regions in the Co–10Al–9W–1C alloy heat treated at 1300 °C for 12 h (*a*) and subsequently aged at 800 °C for 1 h (*b*), 16 h (*c*), 64 h (*d*), and 256 h (*e*), taken using (100) superlattice reflections, for (a) to (c) and (e), and a (110) superlattice reflection, for (d), of the γ'.

Co–10Al–9W–1C alloy aged at 800 °C for 256 hours, the γ' formed a rafted structure similar to that formed in crept samples of certain Ni-base superalloys. Similar structures were reported by other researchers in Co–Al–W alloys[7,25,32,40] and related to the tendency to decrease the elastic strain energy between the γ' precipitates and the matrix.[39] Also, the formation of this microstructure is assisted by the high γ' volume fraction.[13] During rafting, the γ' precipitates merge together and lose their coherency with the matrix, as indicated by the misfit dislocation segments at the γ/γ' interfaces in Figures 8(a) and (b). In addition, the needle-like B2 phase in the dendritic regions (Figures 3(g) and (h)) is shown in Figure 8(b). The Kurdjumov–Sachs (K–S) orientation relationship (OR) between the B2 and the γ/γ' phases[41] is also clear in the SAD patterns in Figure 8(b). Figures 8(c) and (d) show bright-field two-beam images and corresponding SAD patterns of the coarse γ' layers in the microstructure of the Co–10Al–9W–1C alloy aged for 256 hours. As can be seen in the images and SAD patterns (inset in Figure 8(d)), the coarse γ' layers contain both stacking faults (SFs) and twins, due to its low stacking fault energy.[16,20]

2. *Co–7Al–5W and Co–7Al–5W–1C alloys*

In order to investigate the effect of C on the two-phase γ/γ' microstructures and to remove the interdendritic phases which could be deleterious for the mechanical properties,[23] the microstructures of the Co–7Al–5W and Co–7Al–5W–1C alloys were studied during aging at 800 °C. Figures 9(a) and (d) depict SEM microstructures of the Co–7Al–5W and Co–7Al–5W–1C alloys, respectively, after homogenization at 1300 °C for 12 hours. The SEM images (Figures 9(a) and (d)), and EDS analyses (shown in electronic supplementary Figures S1 and S2) indicate that the microstructures have been homogenized by this heat treatment. The higher and lower magnification images in Figures 9(b), (c), (e), and (f) show that the microstructures of the alloys consist only of the γ' precipitation in the γ matrix, while there is no precipitation of the deleterious phases during aging at 800 °C.

Dark-field TEM images of the Co–7Al–5W and Co–7Al–5W–1C alloys aged at 800 °C for 16 and 64 hours (Figure 10) indicate that the γ' area fraction in the C-doped and C-free alloys are 29 and 16 pct, respectively. Therefore, the γ' volume fraction in the Co–7Al–5W alloy at 800 °C is almost doubled by alloying with 1 pct carbon. Also, the γ' precipitates in the microstructures of the alloys aged for 16 hours coarsen during further aging at 800 °C up to 64 hours, as expected. However, the sizes of the γ' precipitates in the quaternary alloy are smaller than those in the ternary alloy (Table III). Therefore, the γ' coarsening rate in the Co–Al–W system appears to have been reduced by additions of carbon despite the increase in the γ' volume fraction.
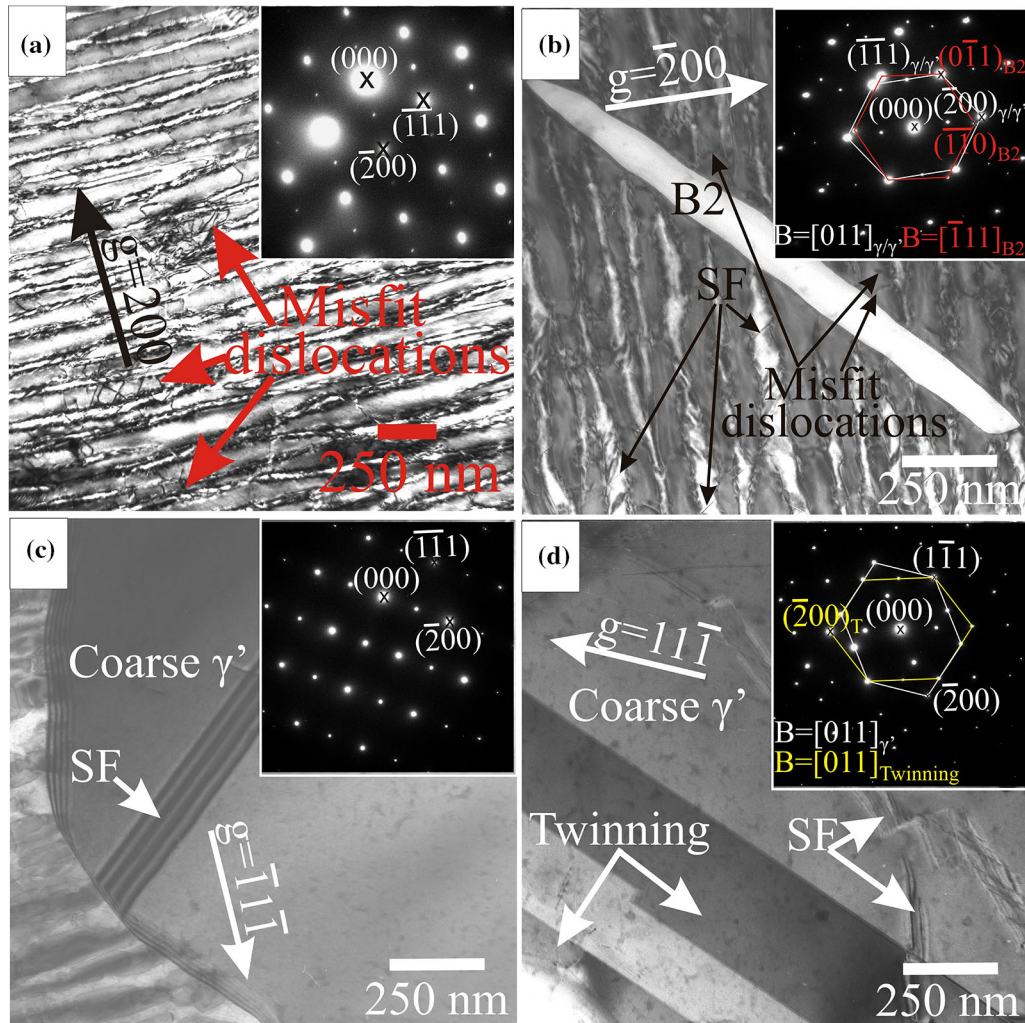
Fig. 8—Bright-field TEM images and corresponding SAD patterns of the Co–10Al–9W–1C sample aged at 800 °C for 256 h, showing the γ' rafted structure (*a*), along with the needle-like B2 precipitates (*b*), and the coarse γ' layers containing stacking faults (*c*) and twins (*d*). The images in (a) to (d) were taken in two-beam conditions using the [200], [$\bar{2}$00], [$\bar{1}1\bar{1}$], and [11$\bar{1}$] g-vectors, respectively, of the γ/γ'.

B. *EDS Analyses*

STEM EDS analyses were conducted on the Co–7Al–5W and Co–7Al–5W–1C alloys aged at 800 °C for 64 hours to measure the compositions of the γ and γ' phases. Figure 11 shows the high-angle annular dark-field (HAADF) STEM images, EDS elemental mapping, and line scan profiles along the γ/γ' microstructures of the ternary and quaternary alloys. The HAADF images in both of the alloys show that the γ' phase has higher Z compared to the γ matrix. However, the line scans and elemental mapping show that the compositions of the γ/γ' phases are different in the Co–7Al–5W and Co–7Al–5W–1C alloys. The γ' phase in the C-doped alloy has lower W content than that in the C-free alloy. Also, the γ phase in the quaternary alloy has lower Al content than that in the ternary alloy. Similar changes in the partitioning behaviors of Al and W between the γ and γ' have also been reported in the Co–10Al–7.5W–5C alloy compared to Co–Al–W alloys at 900 °C.[28] STEM EDS results from several points in the microstructures of the ternary and quaternary alloys in Table IV show the compositions of the γ and γ' phases. The composition of the γ' phase in the Co–7Al–5W–1C alloy (Table IV) is close to that of the coarse γ' layer in the Co–10Al–9W–1C alloy (Table II) in terms of W content. The measured compositions of the γ and γ' phases in the ternary alloy are also in close agreement with compositions of these phases measured using atom probe tomography (APT) in the Co–9Al–7W and Co–7Al–7W alloys aged at 750 °C and 765 °C, respectively.[25,42]

C. *Coarsening Rate Constant Calculation*

Diffusion-controlled coarsening of precipitates with extremely small volume fractions in multicomponent alloys has been modeled by several researchers, such as Björklund *et al.*,[43] Slezov and Sagalovich,[44] Umanstev and Olson,[45] Morral and Purdy,[46] Hoyt,[47] and Kuemann and Voorhees.[48] The Kuemann and Voorhees model (KV)[48] for coarsening in two-phase ternary systems is more comprehensive than the others, due to
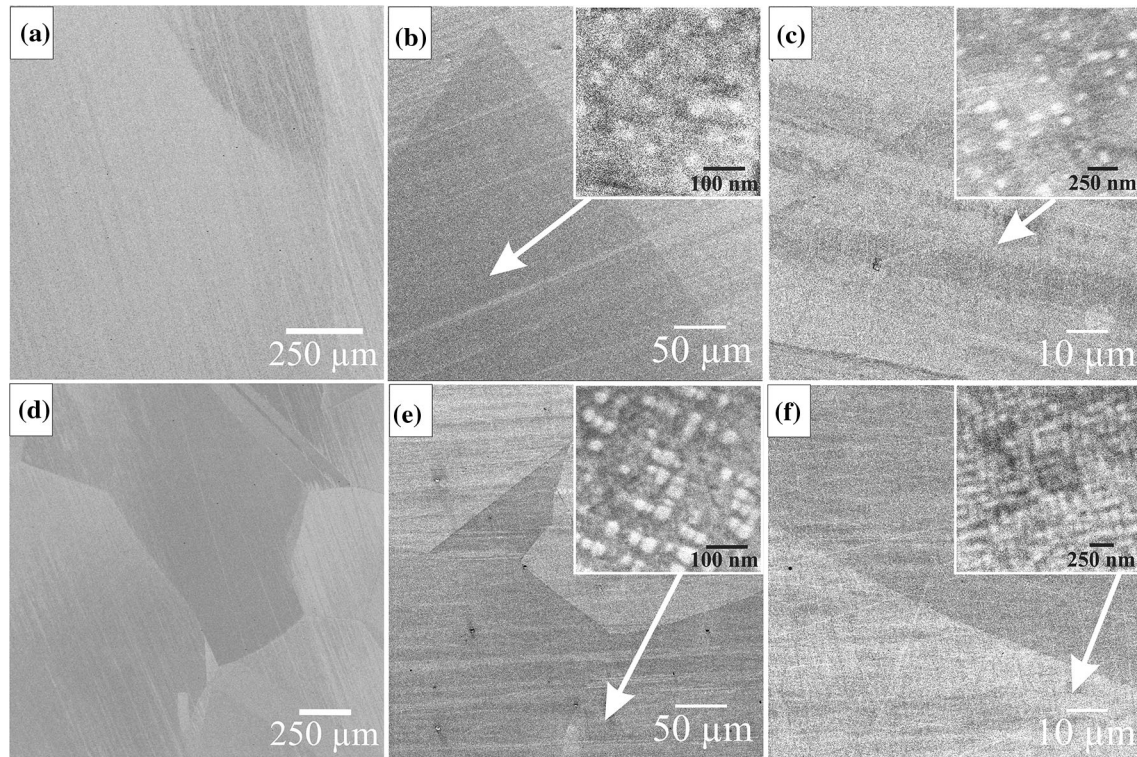
Fig. 9—SEM microstructures of the Co–7Al–5W (*a*) to (*c*) and Co–7Al–5W–1C (*d*) to (*f*) alloys after homogenization at 1300 °C for 12 h (a) and (d), and aging at 800 °C for 16 h (b) and (e) and 64 h (c) and (f). The insets show higher magnification images of the microstructures.

its validity for non-dilute, non-ideal solutions, along with considering the interfacial curvature effects on the precipitate composition. The temporal power law for the average particle size in the KV model[48] is given by

$$r^3 - r_0^3 = Kt \qquad [1]$$

where r is the mean precipitate radius at time t during coarsening, r_0 is the mean precipitate radius at $t = 0$ and K is the coarsening rate constant, which for dilute-ideal solutions is given by

$$K = \frac{8\sigma V_m^\beta}{9RT\left(\frac{C_2^\alpha(1-k_2)^2}{D_2} + \frac{C_3^\alpha(1-k_3)^2}{D_3}\right)} \qquad [2]$$

where σ is the matrix/precipitate interfacial energy, V_m^β is the molar volume of precipitate, R is the universal gas constant ($R = 8.314$ J mol^{-1} K^{-1}), T is the absolute temperature, D_i is the diffusivity of the ith species, k_i is the partitioning coefficient of the ith species defined as C_i^β/C_i^α, and C_i^α and C_i^β are the equilibrium solubilities of the ith species in the matrix and the precipitate, respectively.[48] It is noted that in the case of cubic precipitates, the mean radius of the precipitate (r) is taken as half of the mean edge of the precipitate and is called the mean equivalent radius.[49] This coarsening model could be considered in the investigation of the γ' coarsening in Co–Al–W–C alloys since the direct effect of C partitioning on the coarsening rate would be negligible because of its much higher diffusivity than the other alloying elements in the γ matrix at 800 °C.[30,50,51]

The average equivalent radii (r) of the γ' precipitates in the Co–10Al–9W–1C alloy during aging at 800 °C are included in Table III. In order to identify the coarsening mechanism in the Co–Al–W–C alloys, a log (r) *vs* log (t) plot for the Co–10Al–9W–1C alloy was drawn; Figure 12(a) shows a linear fit for the data points with the slope of 0.307. The slope of this plot determines the inverse of the temporal power which is close to that in Eq. [1] (0.333). Therefore, the coarsening mechanism in this alloy is diffusion controlled similar to other Co–Al–W alloys.[32,52] Figure 12(b) shows r^3 versus aging time plot for the Co–10Al–9W–1C alloy. Also, the data points and fitted line for the Co–10Al–10W alloy[32] have been included to compare with the investigated alloy, due to similarity in their γ' volume fractions (Section III–A–1). The slopes of the linear fits for these data points show the coarsening rate constants (K), according to Eq. [1]. As can be seen in Figure 12(b), the rate constant of the ternary alloy (0.07×10^{-27} m^3 s^{-1}) is decreased significantly by replacing 1 pct W with 1 pct C (0.04×10^{-27} m^3 s^{-1}).

D. Microhardness Measurements

Figure 13 depicts the microhardnesses of the Co–10Al–9W–1C (dendritic regions), Co–7Al–5W–1C, and Co–7Al–5W alloys during aging at 800 °C. Based on this plot, the microhardnesses of the alloys are increased by raising the γ' volume fraction in the microstructures from 16 pct in the Co–7Al–5W alloy to 29 and 78 pct in the Co–7Al–5W–1C and
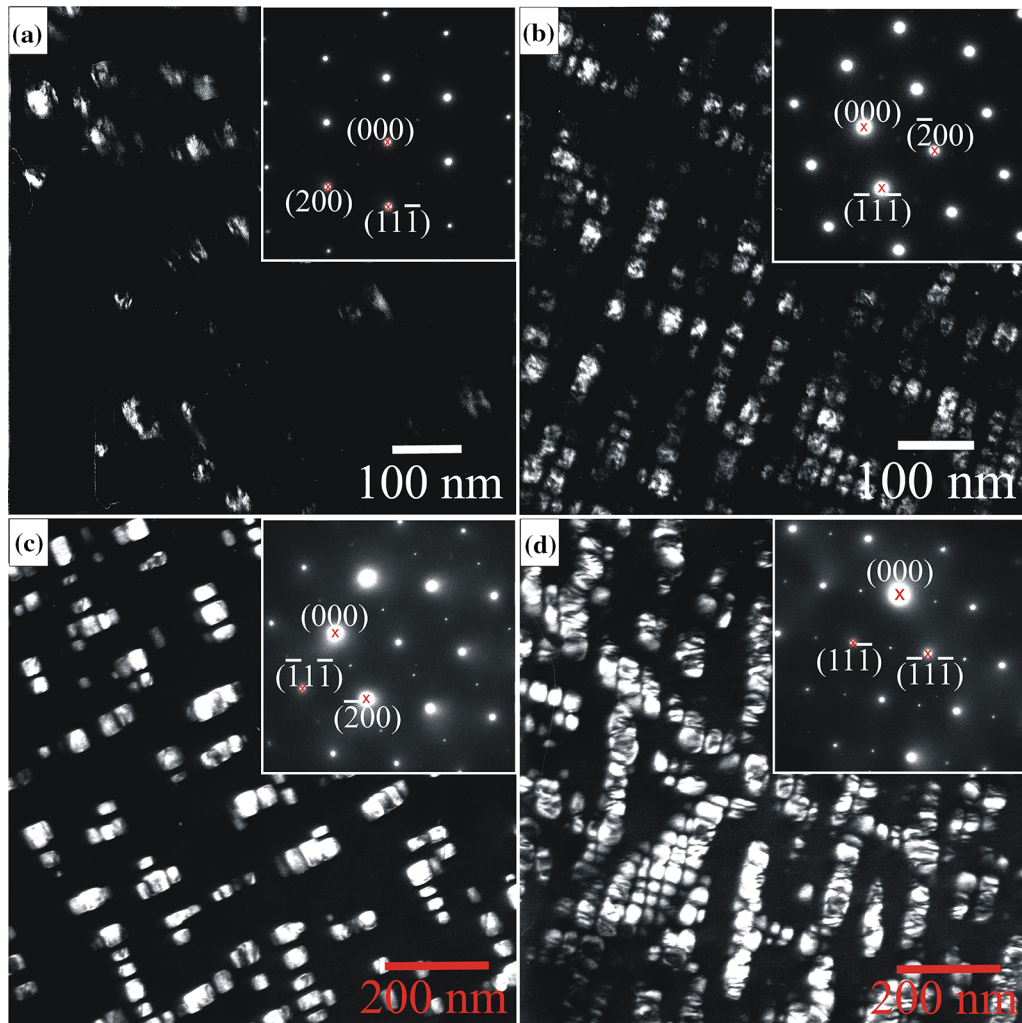
Fig. 10—Dark-field TEM images and corresponding SAD patterns of the Co–7Al–5W (*a*) and (*c*) and Co–7Al–5W–1C (*b*) and *d*) alloys after aging at 800 °C for 16 h (a) and (b) and 64 h (c) and (d). The dark-field images were taken using (100) (a) to (c) and (01-1) (d) superlattice reflections of the γ′.

Table III.   Mean Sizes of the γ′ Precipitates During Aging at 800 °C for Different Alloys

Alloy	Mean Equivalent Radius (nm)				
	0 h	1 h	16 h	64 h	256 h
Co–10Al–9W–1C	4 ± 2	6 ± 3	16 ± 5	22 ± 6	33 ± 10
Co–7Al–5W–1C	—	—	10 ± 4	18 ± 5	—
Co–7Al–5W	—	—	13 ± 4	22 ± 4	—

Co–10Al–9W–1C alloys, respectively (Figures 7 and 10). Also, solid solution strengthening caused by interstitial C atoms is expected to increase the hardness of the C-doped alloys. While the microhardnesses of the Co–7Al–5W–1C and Co–7Al–5W alloys increase upon aging (up to 16 h), they do not show a significant change in the hardness during aging at 800 °C between 16 and 64 hours; however, there is an increase in the micro-hardness of the Co–10Al–9W–1C alloy during aging at

800 °C for the same period of time. Subsequently, the microhardness of the Co–10Al–9W–1C alloy is decreased by aging at 800 °C for 256 hours, due to the coherency loss between the γ and γ′ phases (Figures 8(a) and (b)).

IV.   DISCUSSION

The microstructural investigation of the Co–10Al–9W–1C alloy revealed that the stable η carbide at 1300 °C is unstable at 800 °C and transforms into the $D0_{19}$ phase at this temperature. The micrographs in Figure 1(b) (higher Z phase) and Figure 4 (upper-right image), and the SAD patterns in Figures 2 and 5 show that this transformation does not include any noticeable changes in the location, morphology, and size of the product phase compared to its parent. Also, the EDS results in Tables I and II indicate that the product $D0_{19}$ phase is W supersaturated, which is related to the sluggish diffusivity of W in the surrounding phases
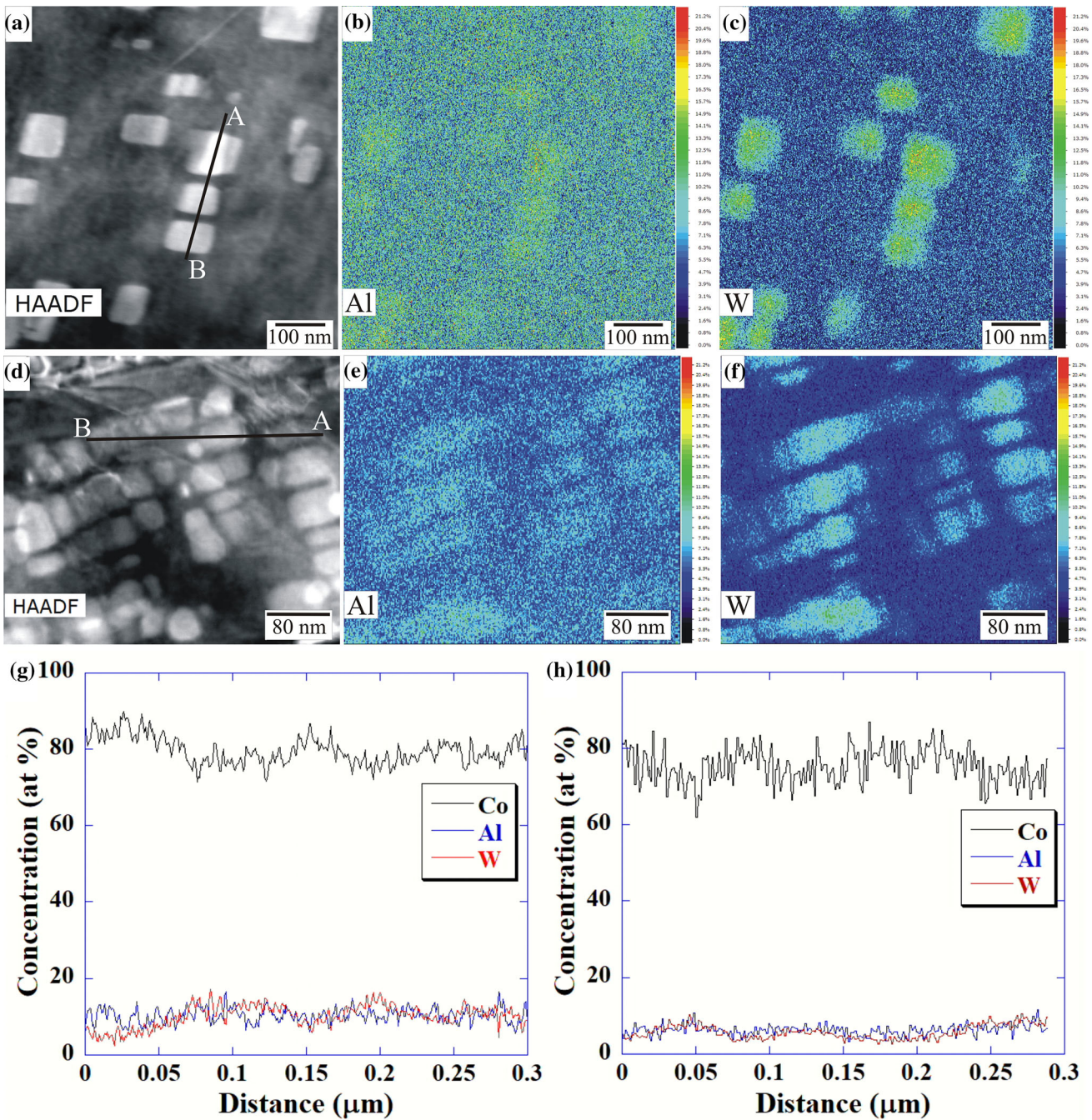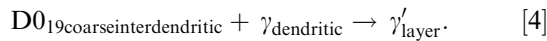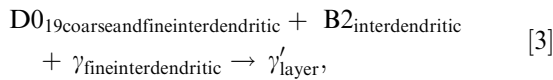
Fig. 11—HAADF-STEM images, EDS elemental mapping and line scan profiles of the Co–7Al–5W (*a*) to (*c*) and (*g*) and Co–7Al–5W–1C (*d*) to (*f*) and (*h*) alloys aged at 800 °C for 64 h: (a) and (d) HAADF images, (b) and (e) Al maps, (c) and (f) W maps, and (g) and (h) line scan profiles along the lines drawn in (a) and (d), respectively.

(Figure 3) at 800 °C,[10,30] making the rejection rate of the W relatively low. It is noted that although decompositions of Ti/Ta-rich MC carbides at the expense of the formation of Cr-rich $M_{23}C_6$[53,54] or W-rich M_6C carbides[55] during prolonged exposures of Ni-base superalloys to high temperatures have been reported, the transformation of the η carbide into the $D0_{19}$ phase has not been observed previously, and more in-depth studies should be conducted on its actual mechanism in the future.

Comparing Figures 3(c) through (h), it is obvious that the product W-supersaturated $D0_{19}$ phase gradually decomposes into the γ' phase during aging at 800 °C. During this decomposition, the γ' layer forms at the interfaces between the decomposing $D0_{19}$ and the interdendritic B2/dendritic regions and grows toward both regions at the expense of the interdendritic B2 phase containing the fine γ and $D0_{19}$ precipitates, and at the expense of the dendritic γ (Figures 3(d), (f) and (h)). This indicates that the $D0_{19}$ phase in the Co–Al–W–C

system is metastable at 800 °C, according to the reactions given by

$$D0_{19\text{coarseandfineinterdendritic}} + B2_{\text{interdendritic}}$$
$$+ \gamma_{\text{fineinterdendritic}} \rightarrow \gamma'_{\text{layer}}, \quad [3]$$

$$D0_{19\text{coarseinterdendritic}} + \gamma_{\text{dendritic}} \rightarrow \gamma'_{\text{layer}}. \quad [4]$$

This observation is in contrast with the previous reports, claiming γ' metastability in ternary Co–Al–W alloys at 850 °C and 750 °C, in which the γ' decomposes into the stable $D0_{19}$, B2, and γ phases,[10,11] and indicates that the addition of 1 pct carbon to the Co–10Al–9W alloy stabilizes the γ' phase at 800 °C.

It is noted that the low C solubilities in the B2 phase[56,57] might explain the initial formation of the fine $D0_{19}$ and γ precipitates, instead of the γ', in the interdendritic B2 regions. However, upon transformation of the η carbide regions, which are in contact with the interdendritic B2, into the coarse $D0_{19}$ during aging at 800 °C, the coarse $D0_{19}$, along with the fine $D0_{19}$ and γ precipitates, and the B2 matrix transform into the γ' (Figure 3 and reaction [3]). Local increase in the C

content at the interface between the η and interdendritic B2 regions during η transformation could increase the stability of the γ' against the $D0_{19}$ at 800 °C, leading to the occurrence of reaction [3].

While it is difficult to measure the carbon concentration in the various phases as mentioned in Section III–A–1, it is possible to speculate on carbon partitioning based on known phase equilibria information. Specifically, the solubility of C in the $D0_{19}$ phase at 800 °C is very low based on Co–W–C isotherms at 1000 °C.[34,35] Further, it is clear that the $D0_{19}$ cannot contain the high C contents of the η-carbide phase. Also, the C solubilities in the dendritic γ and interdendritic B2 phases decrease significantly upon cooling from 1300 °C to 800 °C based on published Co–Al–C isotherms at 1100 °C and 900 °C.[56,57] Given that there is no evidence of carbide formation in the microstructure at 800 °C, it is concluded that the C must partition largely to the γ' phase that (a) precipitates in the dendritic regions and

Table IV. TEM EDS Point Results from the γ and γ' Phases in the Microstructures of the Co–7Al–5W and Co–7Al–5W–1C Alloys Aged at 800 °C for 64 h

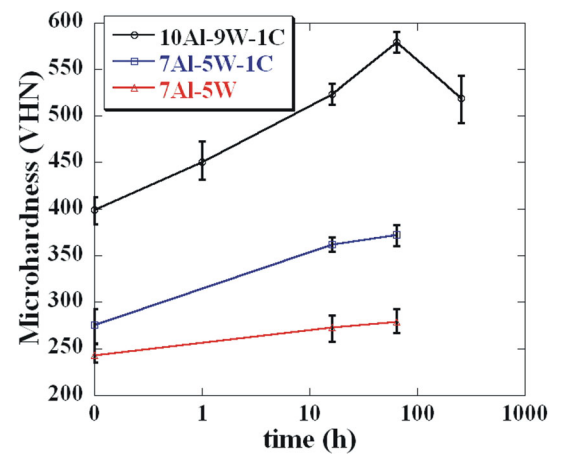| Alloy | Phase | Elemental composition (At. Pct) | | |
		Co	Al	W
Co–7Al–5W	γ	89.3	7.3	3.4
	γ'	75.2	10.6	14.2
Co–7Al–5W–1C	γ	89.9	6.7	3.4
	γ'	79.5	10.2	10.3

Fig. 13—Microhardnesses of the Co–10Al–9W–1C (dendritic regions), Co–7Al–5W–1C, and Co–7Al–5W alloys versus aging time at 800 °C.
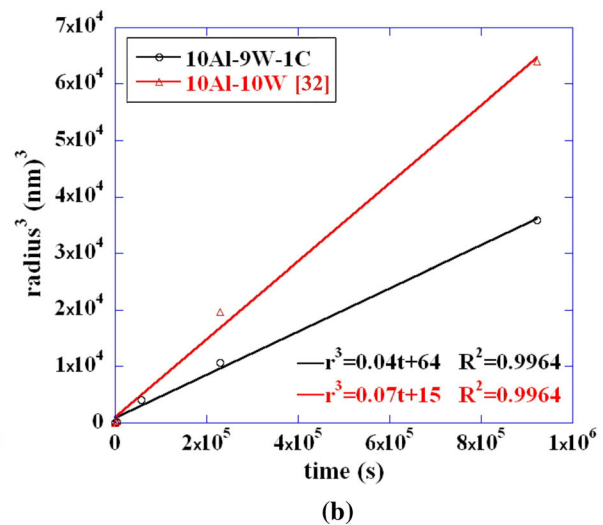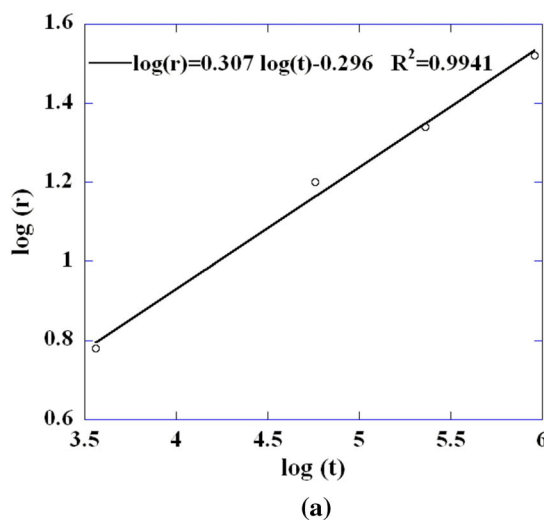

Fig. 12—(a) Log (r) vs Log (t) plot for the Co–10Al–9W–1C alloy, and (b) r^3 against t graph for the Co–10Al–9W–1C and Co–10Al–10W[32] alloys during aging at 800 °C.

(b) forms at the interfaces between the decomposing D0$_{19}$ and the interdendritic B2/dendritic regions (Figures 3, 7, and 8). Also, the lack of carbide precipitation in the microstructure of the Co–7Al–5W–1C alloy supports this conclusion (Figure 9). Regarding the carbon contents of the γ' phase in the C-doped alloys, the maximum possible C content in the γ' phase in the Co–7Al–5W–1C alloy at 800 °C would be about 3.4 pct based on a simple mass conservation analysis, assuming zero solubility of C in the γ phase, and considering the γ' volume fraction. It should also be noted that the maximum possible C concentration in the γ' in the Co–10Al–9W–1C alloy would be even lower than 3.4 pct, due to its much higher γ' volume fraction. Tables II and IV show that the compositions of the γ' phase are Co–12.4Al–10.1W and Co–10.2Al–10.3W in the Co–10Al–9W–1C and Co–7Al–5W–1C alloys, respectively, which indicate offsets from its nominal composition (Co$_3$(Al,W)). In other words, the W contents of the γ' phase are decreased by additions of C compared with the ternary Co–Al–W alloys.

Since the stability of the Co$_3$Al (L1$_2$) phase is improved by alloying with C and W as the κ-Co$_3$AlC and γ'-Co$_3$(Al,W) phases, respectively, with similar structures,[7,27] it is expected that C and W in the Co–Al–W–C system would have a synergistic effect in stabilizing the Co$_3$Al (L1$_2$) phase by partitioning to the γ' phase. As a result, the need for W to stabilize the γ' phase is decreased by C additions to the ternary system[28] (Tables II and IV), and the γ' forms as a stable phase in the Co–Al–W–C system (Figures 3(c) through (h)) with higher volume fractions than the ternary alloys at 800 °C (Figures 7, 8, and 10). Thus, further studies on the phase equilibria in the Co–Al–W–C system will be useful.

Comparing the coarsening behavior of the γ' precipitates in the Co–10Al–10W and Co–10Al–9W–1C alloys, both with similar γ' volume fractions, it is clear that the coarsening rate in the ternary alloy[32] is lowered significantly by replacing 1 pct W with 1 pct C (Figure 12(b)). Based on these results, despite the fact that the additions of C to the Co–Al–W system decrease the W contents of the γ' phase (Tables II and IV),[25,42] the coarsening rate constant is reduced, probably due to a reduction in the γ/γ' interfacial energy (Eq. [2]), resulting from the γ/γ' composition change. However, density functional theory (DFT) calculations are needed to confirm this argument.

Due to the increase in the γ' volume fractions, the microhardnesses of the Co–Al–W alloys are also increased by alloying with C (Figure 13). On the other hand, although there is no significant variation in the volume fraction of the γ' in the dendritic regions of the Co–10Al–9W–1C alloy during aging at 800 °C (Figures 7(b) through (e)), the microhardness of this alloy increases until 64 hours aging. This indicates that the γ' precipitates remain coherent with the γ matrix, and the reason for the microhardness increase is related to the development of coherency strain fields in the γ matrix surrounding the γ' precipitates (the γ' is harder than the γ[39]) during aging until 64 hours. The γ'

precipitates are very close to each other in the microstructure of the Co–10Al–9W–1C alloy aged for 1 hour (Figure 7(b)), as a result of their high volume fraction and small average size (~6 nm), leading to the overlap and cancellation of the coherency strain fields in the γ matrix[39]; however, the mean distance between the γ' precipitates increases along with the γ' coarsening during further aging of the Co–10Al–9W–1C alloy (Figures 7(b) through (d)), assisting the γ' precipitates in further development of their coherency strain fields until 64 hours aging. This proposed mechanism for the microhardness increase is consistent with the microhardness decrease of the Co–10Al–9W–1C alloy during further aging for 256 hours due to the coherency loss between the γ/γ' (Figures 8(a) and (b)). Also, the Co–10Al–9W–1C alloy shows a maximum value of about 600 VHN, which has not been reported previously in other studies on the ternary alloys.[7,23] Moreover, the hardness data in Figure 13 indicate that the strengths of Co–Al–W alloys could also be improved significantly by additions of C. However, the effect of C dissolution in the γ' on the mechanical properties of Co–Al–W alloys, especially creep, is unknown and should be investigated.

Another important effect of C additions in the Co–Al–W system is a reduction in density of the alloys without sacrificing strength, which is important from an industrial applications standpoint.[25] For example, the γ' volume fraction, hardness, and density of Co–7Al–7W–20Ni alloy aged at 790 °C are 27 pct, 348 VHN, and 9.29 g cm^{-3}, respectively.[23] The values of the γ' volume fraction and hardness for this alloy are slightly lower than those for the Co–7Al–5W–1C alloy (29 pct and 372 VHN); however, the density of the latter is about 8.89 g cm^{-3}. Thus, the Co–7Al–5W–1C alloy is approximately 4 pct lighter than the Co–7Al–7W–20Ni alloy, and its density is comparable with those of commercial Ni-base superalloys.[25]

Finally, based on this study, C has tremendous effects on the microstructural stability and hardness of Co–Al–W alloys. Consequently, Co–Al–W–C alloys with the stable γ/γ' microstructures and high specific strengths have considerable potential as high-temperature materials.

V. CONCLUSIONS

Based on the microstructural characterization and microhardness measurements, the phase equilibria in the Co–Al–W system and the hardness of the ternary alloys are changed significantly by additions of C, as summarized below:

1. The η carbide exists in the microstructure of the Co–10Al–9W–1C alloy at 1300 °C and subsequently transforms into the W-supersaturated D0$_{19}$ phase upon aging at 800 °C.
2. The decomposition of the D0$_{19}$ phase into the γ' phase takes place in the Co–10Al–9W–1C alloy during aging at 800 °C, indicating the stability of the γ' in the Co–Al–W–C system at 800 °C in contrast to the Co–Al–W system.

3. The EDS analyses indicate that the W contents of the γ' are decreased by additions of C to the Co–Al–W alloys. This shows that the need for W to stabilize the Co_3Al (L1$_2$) phase is lowered by C additions. Also, it is a reason for the increase in the γ' volume fraction in the quaternary alloys.
4. The coarsening rates of the γ' precipitates in the Co–Al–W–C alloys are lower than those in the Co–Al–W alloys.
5. The microhardnesses of the C-doped alloys are higher than those of the C-free alloys, due to the higher γ' volume fractions. Also, the densities of the Co–Al–W alloys are lowered by replacing W with C without sacrificing the hardnesses.

ACKNOWLEDGMENTS

SUPPLEMENTARY INFORMATION

The online version contains supplementary material available at https://doi.org/10.1007/s11661-021-06470-8.

REFERENCES

1. C.T. Sims: *J. Met.*, 1969, vol. 21, pp. 27–42.
2. A.M. Beltran:Cobalt-base alloys in *Superalloys II*, C.T. Sims, N.S. Stoloff, and W.C. Hagel, eds., Wiley, New York, 1987, 2nd ed., pp. 135–63.
3. R.V. Miner:Fatigue in *Superalloys II*, C.T. Sims, N.S. Stoloff, and W.C. Hagel, eds., Wiley, New York, 1987, 2nd ed., pp. 263–89.
4. L.J. Huetter and H.H. Stadelmaier: *Acta Metall.*, 1958, vol. 6, pp. 367–70.
5. H. Kamali, S. Hossein Nedjad, M.J. Kaufman, R.D. Field, and A.J. Clarke: *Metall. Mater. Trans. A*, 2018, vol. 49A, pp. 3198–3205.
6. C.S. Lee: *Precipitation-Hardening Characteristics of Ternary Cobalt-Aluminum-X Alloys*, Ph.D. Thesis, University of Arizona, 1971, pp. 53–61.
7. J. Sato, T. Omori, K. Oikawa, I. Ohnuma, R. Kainuma, and K. Ishida: *Science*, 2006, vol. 312, pp. 90–91.
8. S. Kobayashi, Y. Tsukamoto, T. Takasugi, H. Chinen, T. Omori, K. Ishida, and S. Zaefferer: *Intermetallics*, 2009, vol. 17, pp. 1085–89.
9. J.E. Saal and C. Wolverton: *Acta Mater.*, 2013, vol. 61, pp. 2330–38.
10. E.A. Lass, M.E. Williams, C.E. Campbell, K.-W. Moon, and U.R. Kattner: *J. Phase Equilib. Diff.*, 2014, vol. 35, pp. 711–23.
11. E.A. Lass, R.D. Grist, and M.E. Williams: *J. Phase Equilib. Diff.*, 2016, vol. 37, pp. 387–401.
12. L. Zhu, C. Wei, H. Qi, L. Jiang, Z. Jin, and J.-C. Zhao: *J. Alloys Compds.*, 2017, vol. 691, pp. 110–18.
13. Y. Li, F. Pyczak, M. Oehring, L. Wang, J. Paul, U. Lorenz, and Z. Yao: *J. Alloys Compds.*, 2017, vol. 729, pp. 266–76.
14. A. Suzuki and T.M. Pollock: *Acta Mater.*, 2008, vol. 56, pp. 1288–97.
15. N.L. Okamoto, T. Oohashi, H. Adachi, K. Kishida, H. Inui, and P. Veyssière: *Philos. Mag.*, 2011, vol. 91, pp. 3667–84.
16. A. Suzuki, H. Inui, and T.M. Pollock: *Annu. Rev. Mater. Res.*, 2015, vol. 45, pp. 345–68.
17. A. Bauer, S. Neumeier, F. Pyczak, and M. Göken: *Scr. Mater.*, 2010, vol. 63, pp. 1197–1200.
18. A. Bauer, S. Neumeier, F. Pyczak, R.F. Singer, and M. Göken: *Mater. Sci. Eng. A*, 2012, vol. 550, pp. 333–41.
19. M.S. Titus, A. Mottura, G.B. Viswanathan, A. Suzuki, M.J. Mills, and T.M. Pollock: *Acta Mater.*, 2015, vol. 89, pp. 423–37.
20. M.S. Titus, Y.M. Eggeler, A. Suzuki, and T.M. Pollock: *Acta Mater.*, 2015, vol. 82, pp. 530–39.
21. I. Povstugar, C.H. Zenk, R. Li, P.-P. Choi, S. Neumeier, O. Dolotko, M. Hoelzel, M. Göken, and D. Raabe: *Mater. Sci. Technol.*, 2016, vol. 32, pp. 220–25.
22. L. Klein, B. von Bartenwerffer, M.S. Killian, P. Schmuki, and S. Virtanen: *Corros. Sci.*, 2014, vol. 79, pp. 29–33.
23. H.-Y. Yan, V.A. Vorontsov, and D. Dye: *Intermetallics*, 2014, vol. 48, pp. 44–53.
24. H.-Y. Yan, V.A. Vorontsov, and D. Dye: *Corros. Sci.*, 2014, vol. 83, pp. 382–95.
25. D.C. Dunand, D.N. Seidman, C. Wolverton, J.E. Saal, P.J. Bocchini and D.J. Sauza: *Designing Nanoscale Precipitates in Novel Cobalt-Based Superalloys to Improve Creep Resistance and Operating Temperature*, Final Technical Report, Northwestern University, Illinois, 2014, pp. 1–25.
26. A.J. McAlister:Al-Co binary phase diagram in *ASM Handbook, Alloy Phase Diagrams*, H Baker, ed., ASM International, Ohio, 1992, vol. 3, p. 2.43.
27. C. Jiang: *Phys. Rev. B*, 2008, vol. 78, pp. 064206-1–6.
28. L.P. Freund, A. Bauer, L. Benker, S. Neumeier, and M. Göken: *Adv. Eng. Mater.*, 2015, vol. 17, pp. 1113–18.
29. W.S. Rasband, *ImageJ*, U. S. National Institutes of Health, Bethesda, Maryland, https://imagej.nih.gov/ij/, 1997–2018.
30. Y.-W. Cui, G. Xu, R. Kato, X.-G. Lu, R. Kainuma, and K. Ishida: *Metall. Mater. Trans. A*, 2013, vol. 44A, pp. 1621–25.
31. I. Povstugar, P.-P. Choi, S. Neumeier, A. Bauer, C.H. Zenk, M. Göken, and D. Raabe: *Acta Mater.*, 2014, vol. 78, pp. 78–85.
32. S. Meher, S. Nag, J. Tiley, A. Goel, and R. Banerjee: *Acta Mater.*, 2013, vol. 61, pp. 4266–76.
33. D.V. Suetin, I.R. Shein, and A.L. Ivanovskii: *Physica B*, 2009, vol. 404, pp. 3544–49.
34. C.B. Pollock and H.H. Stadelmaier: *C-Co-W Phase Diagram*, ASM Alloy Phase Diagram Database, P. Villars, editor-in-chief; H. Okamoto and K. Cenzual, section editors; http://mio.asminternational.org/apd/, ASM International, Materials Park, Ohio, 2006.
35. A. Markström, B. Sundman and K. Frisk: *C-Co-W Phase Diagram*, ASM Alloy Phase Diagram Database, P. Villars, editor-in-chief; H. Okamoto and K. Cenzual, section editors; http://mio.asminternational.org/apd/, ASM International, Materials Park, Ohio, 2007.
36. T. Hahn:Space-group symmetry in *International Tables for Crystallography*, D.W. Penfold, M.H. Dacombe, S.E. Barnes, and N.J. Ashcroft, eds., Springer, Dordrecht, 2005, pp. 600–703.
37. P.A. Carvalho, P.M. Bronsveld, B.J. Kooi, and J.T.M. De Hosson: *Acta Mater.*, 2002, vol. 50, pp. 4511–26.
38. D.B. Williams and C.B. Carter: *Transmission Electron Microscopy A Textbook for Materials Science*, 2nd ed., Springer, New York, 2009, pp. 392–97.
39. A.M. Jokisaari, S.S. Naghavi, C. Wolverton, P.W. Voorhees, and O.G. Heinonen: *Acta Mater.*, 2017, vol. 141, pp. 273–84.
40. F. Pyczak, A. Bauer, M. Göken, U. Lorenz, S. Neumeier, M. Oehring, J. Paul, N. Schell, A. Schreyer, A. Stark, and F. Symanzik: *J. Alloys Compds.*, 2015, vol. 632, pp. 110–15.
41. A.I. Epishin, N.V. Petrushin, T. Link, G. Nolze, Y.V. Loshchinin, and G. Gerstein: *Russian Metall.*, 2016, vol. 2016, pp. 286–91.
42. S. Meher, H.-Y. Yan, S. Nag, D. Dye, and R. Banerjee: *Scripta Mater.*, 2012, vol. 67, pp. 850–53.
43. S. Björklund, L.F. Donaghey, and M. Hillert: *Acta Metall.*, 1972, vol. 20, pp. 867–74.
44. V.V. Slezov and V.V. Sagalovich: *Sov. Phys. Usp.*, 1987, vol. 30, pp. 23–45.

45. A. Umantsev and G.B. Olson: *Scripta Metall. Mater.*, 1993, vol. 29, pp. 1135–40.
46. J.E. Morral and G.R. Purdy: *Scripta Metall. Mater.*, 1994, vol. 30, pp. 905–08.
47. J.J. Hoyt: *Acta Mater.*, 1999, vol. 47, pp. 345–51.
48. C.J. Kuehmann and P.W. Voorhees: *Mater. Trans. A*, 1996, vol. 27, pp. 937–43.
49. M. Doi: *Prog. Mater. Sci.*, 1996, vol. 40, pp. 79–180.
50. Y. Iijima, F. Makuta, and R.P. Agarwala: *Mater. Trans.*, 1989, vol. 30, pp. 984–90.
51. Y.-W. Cui, B. Tang, R. Kato, R. Kainuma, and K. Ishida: *Metall. Mater. Trans. A*, 2011, vol. 42A, pp. 2542–46.
52. V.A. Vorontsov, J.S. Barnard, K.M. Rahman, H.-Y. Yan, P.A. Midgley, and D. Dye: *Acta Mater.*, 2016, vol. 120, pp. 14–23.
53. G. Lvov, V.I. Levit, and M.J. Kaufman: *Metall. Mater. Trans. A*, 2004, vol. 35A, pp. 1669–79.
54. A.J. Wasson and G.E. Fuchs: *Mater. Charact.*, 2012, vol. 74, pp. 11–16.
55. L.R. Liu, T. Jin, N.R. Zhao, X.F. Sun, H.R. Guan, and Z.Q. Hu: *Mater. Sci. Eng. A*, 2003, vol. 361, pp. 191–97.
56. Y. Kimura, M. Takahashi, S. Miura, T. Suzuki and Y. Mishima: *Al-C-Co Phase Diagram*, ASM Alloy Phase Diagram Database, P. Villars, editor-in-chief; H. Okamoto and K. Cenzual, section editors; http://mio.asminternational.org/apd/, ASM International, Materials Park, Ohio, 2009.
57. B. Grieb and H.H. Stadelmaier: *Al-C-Co Phase Diagram*, ASM Alloy Phase Diagram Database, P. Villars, editor-in-chief; H. Okamoto and K. Cenzual, section editors; http://mio.asminternational.org/apd/, ASM International, Materials Park, Ohio, 2006.